Chemical Engineering Journal 479 (2024) 147401

Contents lists available at ScienceDirect

Chemical Engineering Journal

journal homepage: www.elsevier.com/locate/cej

Few-cycle atomic layer deposition to nanoengineer polybenzimidazole for H_2/CO_2 separation

Leiqing Hu [a,1], Won-Il Lee [b,1], Ashwanth Subramanian [b], Erda Deng [a], Kim Kisslinger [c], Shouhong Fan [d], Vinh T. Bui [a], Yifu Ding [d], Chang-Yong Nam [b,c,*], Haiqing Lin [a,*]

[a] Department of Chemical and Biological Engineering, University at Buffalo, The State University of New York, Buffalo, NY 14260, USA
[b] Department of Materials Science and Chemical Engineering, Stony Brook University, Stony Brook, NY 11794, USA
[c] Center for Functional Nanomaterials, Brookhaven National Laboratory, Upton, NY 11973, USA
[d] Department of Mechanical Engineering, University of Colorado, Boulder, CO 80309, USA

ARTICLE INFO

Keywords:
Atomic layer deposition
Vapor-phase infiltration
AlO_x
Polybenzimidazole
H_2/CO_2 separation membranes

ABSTRACT

Atomic layer deposition (ALD) creates uniform sub-nanometer films on a variety of surfaces and nanopore walls and has been used to modify polymers to improve surface affinity towards specific molecules, solvent resistance, and barrier properties to gases and vapors. Here, for the first time, we demonstrate that few-cycle ALD can be used to engineer functional polymers at a sub-nanometer scale to improve both molecular size-sieving ability and counterintuitively, gas permeability. Particularly, 1-cycle ALD treatment of polybenzimidazole (PBI) by sequential exposure to trimethylaluminum (TMA) and water vapor remarkably increases H_2 permeability by 120% – 270% and H_2/CO_2 selectivity by 30% at 35–200 °C. The ALD not only deposits an AlO_x layer on the surface but also enables the TMA to infiltrate and react with the bulk PBI to form an AlO_x network, disrupting polymer chain packing and increasing chain rigidity. The membrane exhibits excellent stability when challenged with simulated syngas, overcoming the permeability/selectivity tradeoff for H_2/CO_2 separation. This study showcases a facile and scalable way of engineering polymeric membranes at a sub-nanometer level to improve molecular separation performance.

1. Introduction

Functional surface plays a critical role in a variety of applications, and the ability to uniformly deposit angstrom (Å)-scale thin layers is highly desirable. Atomic layer deposition (ALD) has emerged as an attractive approach, as it utilizes reactions between alternative gaseous precursors, depositing dense thin layers with well-controlled thicknesses [1–4]. It can effectively modify the hydrophilicity and chemistries of the dense surface [5,6], fine-tune the pore size and porosity at a molecular level for porous substrates [7–9], and improve the resistance to solvents [10]. As such, ALD has demonstrated the potential to improve polymer performance, such as water treatment [4,11], membrane liquid separations [10,12,13], energy storage [14–16], and catalysts [17].

ALD holds great promise to precisely fine-tune the pore size and thus size-sieving ability in polymeric membranes to improve gas separation performance in a scalable way, partially because commercial membranes comprise very thin selective layers and any modification at nanoscales exerts a significant impact on the overall performance [18–20]. However, ALD has been conventionally used to generate AlO_x layers to improve barrier properties for gases and vapors [21–23], with a few studies on gas separation focused on a polymer of intrinsic microporosity (PIM-1) [18,24]. For instance, PIM-1 was treated with ALD using trimethylaluminum (TMA) and water, and 6-cycle AlO_x deposition decreased the pore size from 6.5 - 8.5 to 6.2 Å and increased CO_2/CH_4 selectivity by 260 % from 15.7 to 56.2 [18]. However, the reduced pore size decreased CO_2 permeability by more than one order of magnitude from 8287 to 624 Barrer (1 Barrer = 10^{-10} cm^3(STP) cm cm^{-2} s^{-1} $cmHg^{-1}$) [24]. On the other hand, an enormous amount of functional polymers have been developed for societally important gas separations, such as H_2/CO_2 separation for clean H_2 purification and pre-combustion CO_2 capture [25,26]. There is a substantial gap in understanding how this exciting ALD nanotechnology may impact the nanostructures of functional polymers and thus gas separation performance.

Here, for the first time, we report a unique and synergistic effect of

* Corresponding authors at: Department of Materials Science and Chemical Engineering, Stony Brook University, Stony Brook, NY 11794, USA.
E-mail addresses: cynam@bnl.gov (C.-Y. Nam), haiqingl@buffalo.edu (H. Lin).
[1] These authors contributed equally to this work.

https://doi.org/10.1016/j.cej.2023.147401
Received 8 September 2023; Received in revised form 27 October 2023; Accepted 13 November 2023
Available online 25 November 2023

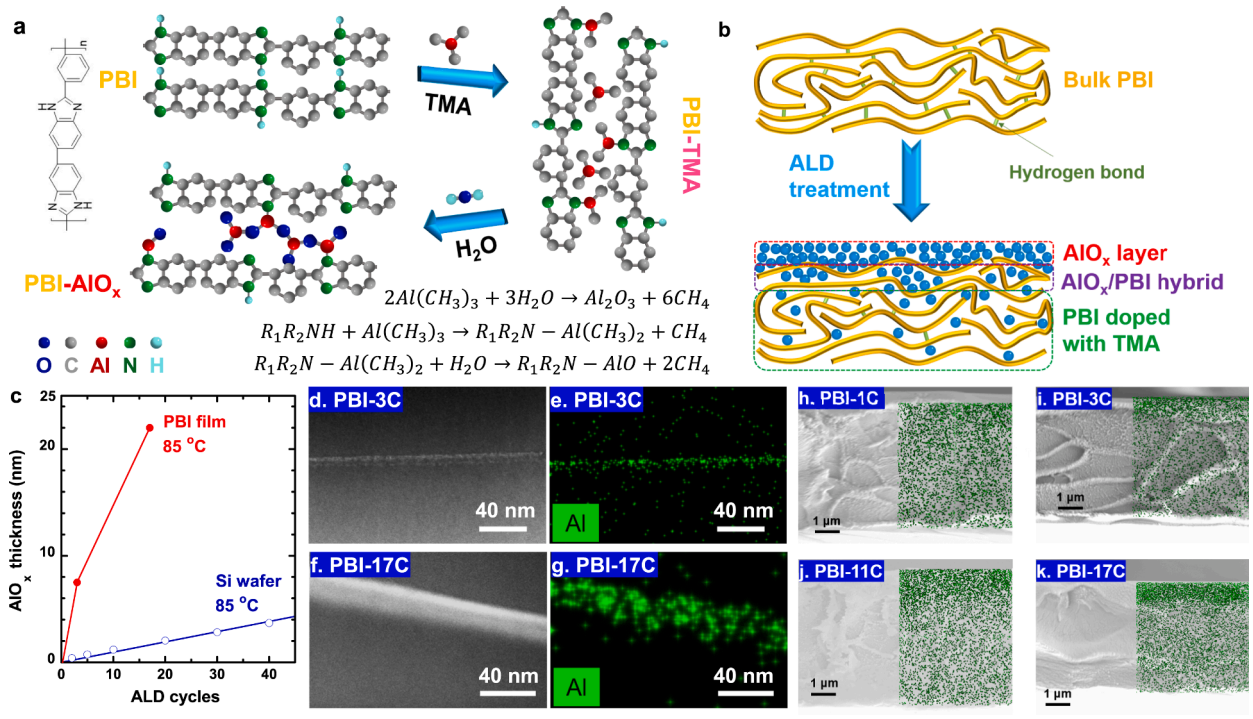

Fig. 1. ALD schematic and morphology for PBI-*x*C. (a) Reactions. (b) Three phases including AlO_x, PBI/AlO_x hybrid, and PBI bulk doped by TMA. (c) AlO_x thickness on Si wafers and PBI films as a function of ALD cycles. Cross-sectional HAADF TEM micrographs of (d) PBI-3C and (f) PBI-17C, and EDS elemental mapping of (e) PBI-3C and (g) PBI-17C. SEM cross-sectional images and in-situ Al EDS mappings of (h) PBI-1C, (i) PBI-3C, (j) PBI-11C, and (k) PBI-17C.

the ALD treatment of polybenzimidazole (PBI, a leading polymer for H_2/CO_2 separation [27,28]) to increase H_2 permeability and H_2/CO_2 selectivity simultaneously. An ALD cycle includes four steps (Fig. S1). First, TMA vapor is introduced and adsorbed onto the PBI film surface, enabling the TMA to diffuse into the film subsurface. Second, the TMA is purged by N_2 flow to remove the TMA from the chamber. Third, water vapor is introduced to bind to the Al atoms on the surface and in the films forming hydroxyl groups, which act as growth sites for AlO_x. Fourth, the N_2 is used to purge out the by-products and residual reactants. By repeating the cycles, an AlO_x layer can grow on the PBI film with a precisely controlled thickness. More importantly, the Lewis-acidic TMA vapor diffuses into the film and reacts with the Lewis-basic amine groups on the PBI chains (Fig. 1a) [7,29–31], inducing new Al-N bonds and an AlO_x network inside the PBI film (i.e., vapor-phase infiltration (VPI) [32]), disrupting the chain packing and influencing the free volume. Consequently, the ALD-treated PBI films comprise three phases (Fig. 1b), including an AlO_x layer on the surface, a dense AlO_x/PBI hybrid layer beneath the surface, and the bulk PBI doped by TMA (i.e., AlO_x). These samples are named PBI-*x*C, where x represents the number of ALD cycles ($x = 1 – 17$ in this study).

We thoroughly investigate the effect of the ALD cycles on both the morphology and H_2/CO_2 separation properties of the PBI membranes. One ALD cycle remarkably increases pure-gas H_2 permeability by 270 % from 2.3 to 8.4 Barrer while retaining H_2/CO_2 selectivity of 12 at 35 °C, and increasing the temperature from 35 to 200 °C increases H_2 permeability of PBI-1C by more than on order of magnitude to 110 Barrer and H_2/CO_2 selectivity by 58 % to 19. The PBI-1C exhibits stable H_2/CO_2 separation performance when challenged with simulated syngas containing water vapor up to 200 °C, surpassing Robeson's upper bound. The significant improvement of H_2/CO_2 separation performance by relatively simple, only a few ALD cycles convincingly demonstrates its potential for industrial applications.

2. Experimental

2.1. Materials

Celazole PBI powder was procured from PBI Performance Products, Inc. (Charlotte, NC). Dimethylformamide (DMF) was acquired from Sigma-Aldrich Corporation (St. Louis, MO). Gas cylinders of N_2, H_2, and CO_2 with ultrahigh purity were purchased from Airgas Inc. (Buffalo, NY).

2.2. Preparation of PBI films and ALD

PBI freestanding films were prepared by casting a solution containing 6 mass% PBI in DMF followed by 48-h drying under vacuum at 150 °C [33]. ALD was conducted using a Veeco Savannah S200 at 85 °C and 0.4 Torr under N_2 environment. Each cycle of depositions includes 15-ms pulsation of TMA as an Al precursor, 10-s N_2 purging, 15-ms pulsation of water vapor as an oxidizer, and 10-s N_2 purging. Multi-cycles can be used to obtain a desired AlO_x thickness on PBI films. For TMA only infiltration, each cycle includes 15-ms pulsation of TMA separated by 10-s N_2 purging.

2.3. Characterization

An M−2000FI ellipsometer (J.A. Woollam Co., Lincoln, NE) was used to determine the AlO_x thickness after various ALD cycles on Si wafers. The spectral reflectance data were collected with incidence angles from 50° to 80° at an angle step size of 10° and wavelengths from 200 to 1600 nm. The thickness was analyzed by the WVASE32 data acquisition and analysis software based on a three-layer model (AlO_x/native SiO_2/Si) and the optical constants of each layer provided by the software.

A dimension icon atomic force microscopy (AFM, Bruker, Germany) was used to record the roughness of the samples in air tapping mode with a probe of TESPA-V2 (Bruker, Germany). A goniometer (Ramé-hart

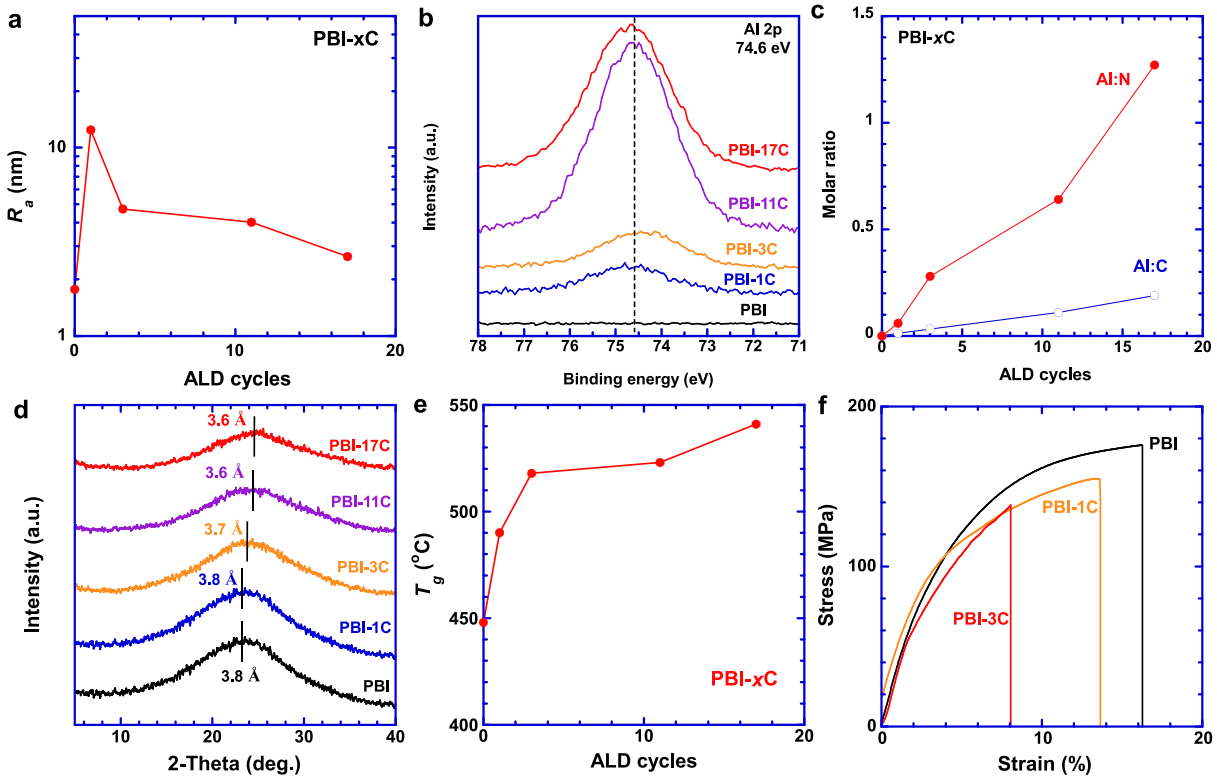

Fig. 2. Physicochemical properties of the PBI-*x*C samples. (a) Surface roughness determined from AFM images. (b) High-resolution XPS spectra of Al 2p, and (c) the molar ratios of Al/C and Al/N. (d) WAXD patterns. (e) Glass transition temperature (T_g). (f) Tensile stress–strain curves.

Instrument, Succasunna, NJ) was used to measure the surface hydrophilicity using water drops of 2 μL. A dynamic mechanical analyzer (DMA) (Q800 TA Instrument) was employed to investigate mechanical properties using static tensile loading. The uniaxial tensile loading on the sample started from 0.1 % and increased by 1.0 %/min until the sample fractured. Three areas of each sample were measured, and average Young's modulus (from the elastic deformation region), tensile strength, and fracture strain were obtained from the stress–strain curves. The curves of thermogravimetric analysis (TGA) and differential scanning calorimetry (DSC) were obtained from an SDT Q600 (TA Instruments, New Castle, DE) from 100 to 800 °C at a ramping rate of 10 °C min^{-1} under a N_2 flow. A Focused Ion Beam Scanning Electron Microscopy (FIB-SEM, Carl Zeiss Auriga CrossBeam, Germany) was used to observe the cross-section, and an EDS (Oxford Instruments, Abingdon, UK) was used to analyze the elemental distribution. The PBI-*x*C samples were characterized using Transmission electron microscope (TEM, FEI Talos, 200 kV), and the cross-sectional samples were prepared using a standard in situ FIB lift-out procedure and Ga ion milling with FEI Helios 600 Nanolab. The elemental compositions were characterized by x-ray photoelectron spectroscopy (XPS) on a custom-built XPS system equipped with a hemispherical electron energy analyzer (SPECS) and Al Ka X-ray source (1486.6 eV).

Pure-gas permeability was determined using a constant-volume and variable-pressure apparatus at 35 and 150 °C [34]. Pure-gas sorption isotherms of CO_2 and C_2H_6 at 35 °C were determined using a gravimetric sorption analyzer of IGA 001 (Hiden Isochema Ltd., Warrington, UK). The uncertainty for gas permeability and solubility is estimated to be < 10 % using an error propagation method [35]. Mixed-gas permeation was performed using a constant-pressure and variable-volume apparatus from 100 to 200 °C.

3. Results and discussion

3.1. Membrane fabrication and characterization

To determine the growth rate of the deposited AlO_x layer on the surface, a control experiment was conducted on Si wafers with ALD cycles of 2 – 40, and their thicknesses were determined using ellipsometry. Fig. 1c shows that the AlO_x layer thickness increases linearly at 0.09 nm/cycle [31].

Fig. 1d-g displays the cross-sectional high-angle annular dark-field (HAADF) scanning transmission electron microscopy (STEM) and energy-dispersive X-ray spectroscopy (EDS) elemental mapping for PBI-3C and PBI-17C, which show an Al-containing layer with a thickness of 7.5 and 22 nm, respectively. These layers are much thicker than pure AlO_x deposited on the Si wafers (0.25 nm at 3 cycles and 1.5 nm at 17 cycles, Fig. 1c) because a significant amount of TMA can infiltrate into PBI, thus forming a dense, AlO_x-infiltrated PBI layer, as evidenced by the sparse, yet uniformly distributed Al signals within the bulk PBI from the EDS mappings (Fig. 1e,g) and the Al EDS mappings from SEM (Fig. 1h-k). The results are consistent with the ALD treatment of PIM-1, where 6 cycles deposited < 1 nm AlO_x on the surface but achieved an infiltration depth of 3–5 μm [7,24], though PIM-1 has much higher fractional free volume (*FFV*, 0.26) than PBI (0.16).

Fig. S1 compares the surface morphology of PBI and PBI-1C using AFM. The PBI film exhibits a smooth surface with a height deviation ranging from –7.6 to 8.2 nm with an arithmetic height average (R_a) of 1.8 nm (Fig. 2a). The 1-cycle ALD dramatically increases R_a to 12 nm likely because the TMA reacts with the amine groups on the surface and etches the surface [31]. The maximum height (R_{max}) and root-mean-squared average of the height (R_q) also increase significantly (Fig. S2f). However, a further increase in the number of ALD cycles decreases the surface roughness (Fig. S2) because of the uniform deposition of the AlO_x layer via true ALD mode (as opposed to VPI) and the planarization of the surface [31].

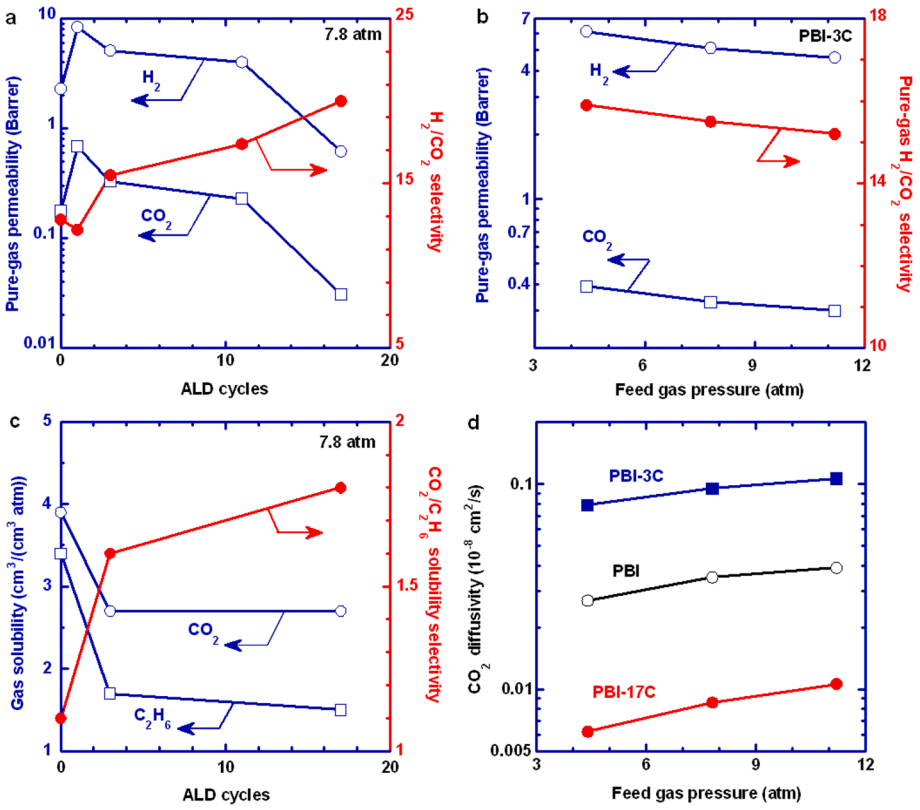

Fig. 3. Pure-gas H_2/CO_2 separation properties of PBI-*x*C at 35 °C. H_2/CO_2 separation properties for (a) PBI-*x*C as a function of ALD cycles at 7.8 atm, and (b) PBI-3C as a function of feed gas pressure. (c) CO_2 and C_2H_6 solubility at 7.8 atm and (d) CO_2 diffusivity as a function of feed gas pressure.

Surface chemistry of the PBI-*x*C films was characterized using XPS. All samples exhibit characteristic peaks of C 1 s (285 eV), N 1 s (399 eV), and O 1 s (532 eV) (Fig. S3). The abnormally high O content in the samples can be ascribed to the –OH groups formed on the surface and water molecules adsorbed on the surface [36]. The ALD treatment increases the Al 2p peak at 75 eV and decreases the N 1 s peak at ~ 400 eV (Fig. 2b). The 17-cycle treatment increases the Al/C molar ratio from 0 to 0.19 and the Al/N ratio from 0 to 1.3 and decreases the N/C from 0.23 to 0.15 (Table S1), confirming the formation of the AlO_x layer on the surface. Additionally, the PBI-*x*C surface displays similar water contact angles (WCAs) at ≈ 90° (Fig. S4), indicating that the ALD has a negligible impact on the hydrophilicity because of the thin AlO_x layers produced in this study.

Fig. 2d compares the wide-angle X-ray diffraction (WAXD) patterns of PBI-*x*C samples. There is an absence of sharp peaks for crystalline structures probably because the crystalline AlOx layer is too thin to determine [18]. The broad peak on the PBI pattern at 23.2° corresponds to a *d*-spacing (representing an average intersegmental distance between the polymer chains) of 3.8 Å calculated using Bragg's law [37]. The *d*-spacing decreases slightly with increasing ALD cycles, as the TMA (<5.4 Å [24]) interacts with the amine groups, narrows the free volume at the subnanometer scale, and tightens the polymer nanostructures. The results are also consistent with the increased density with increasing ALD cycles (Fig. S5a).

The TGA curves of the PBI-*x*C films almost overlap that of the pristine PBI (Fig. S5c), indicating that the ALD has a negligible effect on thermal stability. The glass transition temperature (T_g) can be determined from the DSC curves (Figs. S5d and 2e). The pristine PBI exhibits a T_g value of 448 °C, consistent with the literature data [38,39]. Interestingly, one and three cycles of ALD treatment increase the T_g significantly to 490 and 519 °C, respectively, indicating the enhanced chain rigidity throughout the bulk and confirming the TMA infiltration of the bulk PBI (Fig. 1e,g). Since normal ALD would add only < 10 nm AlO_x layers on the surface of the 8-μm films, the increased T_g value further confirms that in our ALD process, TMA is not only adsorbed on the surface but also penetrates into the bulk films via VPI mode, reacting with the polymer chains [40].

Fig. 2f compares the stress–strain curves of PBI, PBI-1C, and PBI-3C. The AlO_x deposition has a minimal effect on Young's modulus but decreases tensile strength, fracture strain, and toughness (Table S2), which are similar to the ALD-treated PIM-1 [24]. This result suggests increased chain rigidity, validating the TMA infiltration and reaction with the bulk PBI [40]. Notably, 3-cycle ALD significantly decreases the fracture strain from 18 % to 8.1 % and toughness from 2600 to 760 MJ/m^3, consistent with the dramatic change in gas permeation properties.

3.2. Gas transport properties and separation mechanism

Fig. 3a exhibits pure-gas H_2 and CO_2 permeability of PBI-*x*C of ≈ 8.0 μm at 7.8 atm and 35 °C. PBI shows H_2 permeability of 2.3 Barrer and H_2/CO_2 selectivity of 12, consistent with the literature [28,41]. 1-cycle ALD increases H_2 permeability by 270 % to 8.4 Barrer while retaining H_2/CO_2 selectivity. As a comparison, we also treat the PBI films with TMA pulsing only and observe a similar trend of increasing gas permeability (Fig. S6a), suggesting the importance of the reaction between TMA and PBI. The dramatic TMA sorption during initial ALD cycles has also been reported for other polymers, such as polymethylmethacrylate (PMMA), polypropylene (PP), and poly(vinyl chloride) (PVC) [31]. On the other hand, both PBI and PBI-1C exhibit the same *d*-spacing value (Fig. 2d), suggesting that the TMA may not increase free volume but impact the free volume distribution to increase gas permeability. Further increase in ALD cycles decreases gas permeability and increases H_2/CO_2 selectivity because the decreasing *d*-spacing becomes more dominant. For instance, PBI-17C exhibits H_2 permeability of 0.62 Barrer and H_2/CO_2 selectivity of 20. The decreased permeability can also be partially ascribed to the increased thickness of the AlO_x layer on the

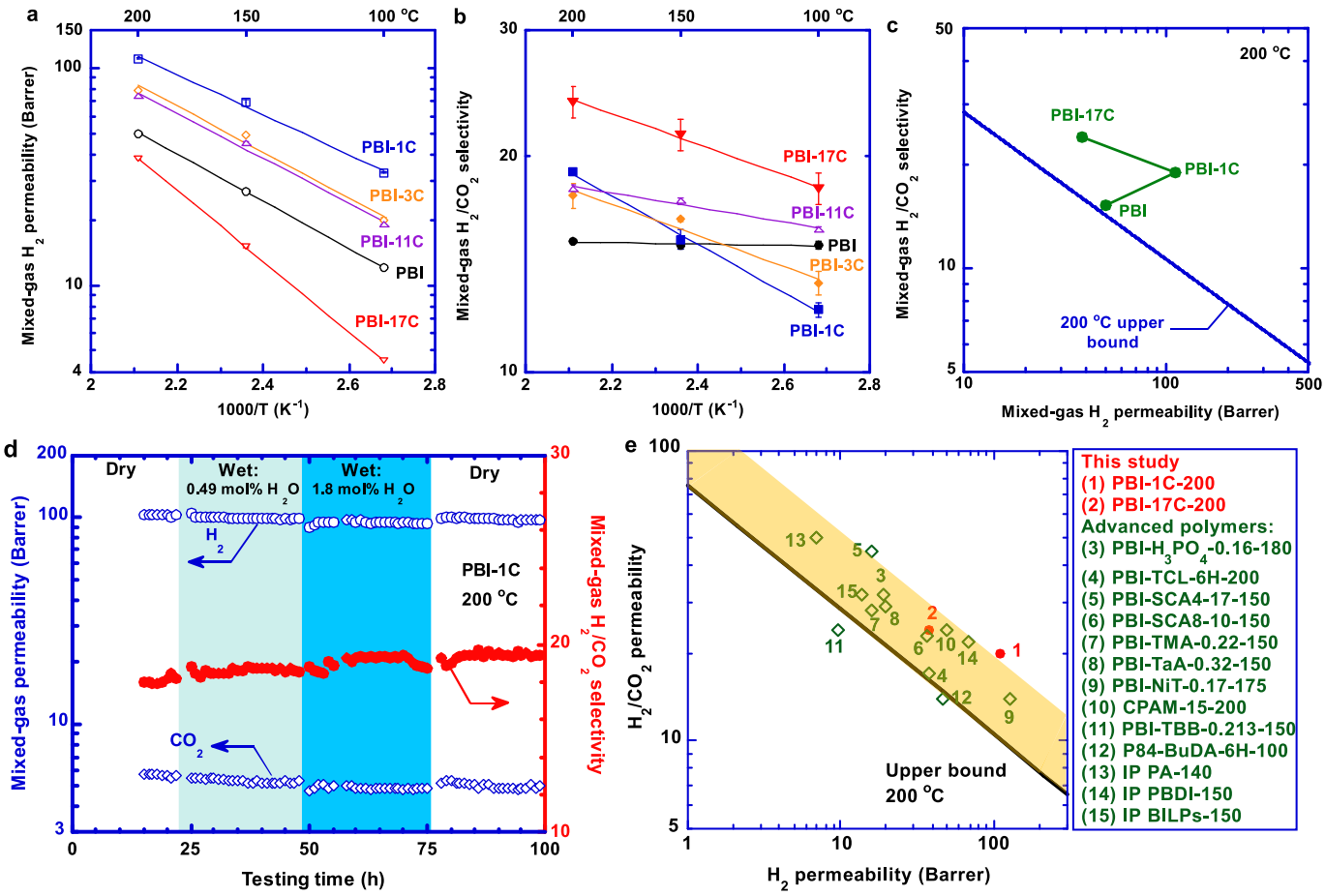

Fig. 4. Superior mixed-gas H_2/CO_2 separation performance with H_2/CO_2 of 50:50 in PBI-xC. (a) H_2 permeability and (b) H_2/CO_2 selectivity as a function of temperature. (c) Comparison with Robeson's upper bound at 200 °C. (d) Long-term stability of PBI-1C in dry-wet-dry conditions at 7.8 atm and 200 °C for 100 h. (e) Comparison with state-of-the-art polymeric materials (Table S5), including PBI-(H_3PO_4)-0.16 [28], PBI-TCL-6H [38], PBI-SCA4-17 [42], PBI-SCA8-10 [27], PBI-TMA-0.22 [41], PBI-TaA-0.32 [37], PBI-NiT-0.17 [43], CPAM-15 [33], PBI-TBB-0.213 [44], P84-BuDA-6H [45], IP PA [46], IP PBDI [47], and IP BILPs [48]. The last number in the sample names represents the testing temperatures (°C).

surface and the increased resistance to gas transport [21,22].

Fig. 3b illustrates the pressure dependency of H_2/CO_2 separation properties of PBI-3C at 35 °C. Gas permeability decreases with increasing feed pressure, which can be described by the dual-mode sorption model, where the Langmuir sorption sites become saturated at high pressures. In contrast, this behavior differs from that of the pristine PBI (Fig. S6b), presumably because the PBI-3C has lower free volumes and is easier to be saturated than PBI. Additionally, H_2/CO_2 selectivity remains almost unchanged with increasing pressure in PBI-3C.

Gas permeability can be decoupled into solubility and diffusivity to elucidate the transport mechanism. As H_2 sorption in PBI is too low to determine using our apparatus, C_2H_6 is chosen as its surrogate, as neither has specific interactions with PBI or AlO_x. The CO_2 and C_2H_6 sorption isotherms at 35 °C can be satisfactorily described using the dual-mode sorption model (Eq. S1) (Fig. S6c,d) with the adjustable parameters recorded in Table S3. The ALD decreases CO_2 solubility by 30 % and C_H' values regardless of the cycle number, indicating a decreased Langmuir sorption capacity caused by the reduced free volume. Interestingly, the C_H' value for C_2H_6 decreases significantly from 26 to 1.0 $cm^3(STP)\ cm^{-3}$ with increasing ALD cycles, indicating that the Langmuir cavities gradually become inaccessible to C_2H_6 because of the reduced free volume size. As such, CO_2/C_2H_6 solubility selectivity increases with increasing ALD cycles. The sorption behavior further validates the TMA infiltration and commensurate decrease in free volumes of the bulk PBI.

Fig. 3d depicts that 3-cycle ALD increases CO_2 diffusivity by 170 % from 3.5×10^{-10} to 9.5×10^{-10} cm^2/s at 35 °C, but a further increase to 17 cycles decreases CO_2 diffusivity to 8.6×10^{-11} cm^2/s, reflecting the competing effects of the disrupted chain packing by the infiltrated TMA and the reduced free volume by the AlO_x network and TMA cross-linking. The ALD treatment mainly affects CO_2 diffusivity, instead of CO_2 solubility. Such an effect is expected to be similar for H_2 transport, though it cannot be directly validated because of the lack of H_2 sorption data.

3.3. Superior H_2/CO_2 separation performance

PBI-*x*C samples are further evaluated with a H_2/CO_2 (50/50 vol%) mixture at 100–200 °C. Both H_2 permeability (Fig. 4a) and CO_2 permeability (Fig. S6e) increase with increasing temperature, which can be described using the Arrhenius equation (Eq. S2) with the fitting parameters recorded in Table S4. The activation energy for permeation (E_P) slightly decreases before increasing with increasing ALD cycle, consistent with the trend of gas permeability. Surprisingly, different from the pristine PBI, the PBI-*x*C exhibits E_P values higher for H_2 than for CO_2 probably because of the enhanced polymer chain rigidity, leading to an increased H_2/CO_2 selectivity with increasing temperature (Fig. 4b). For instance, PBI-1C exhibits H_2 E_P of 18 kJ/mol (higher than CO_2 E_P of 11 kJ/mol), leading to an increased H_2/CO_2 selectivity from 12 at 35 °C to 19 at 200 °C.

Fig. 4c compares mixed-gas performance of PBI, PBI-1C, and PBI-17C

at 200 °C with Robeson's upper bound. PBI-1C has an excellent combination of H_2 permeability and H_2/CO_2 selectivity, surpassing the upper bound. Therefore, it was chosen to investigate the long-term stability using simulated syngas containing water vapor up to 1.8 mol % at 200 °C. PBI-1C exhibits stable mixed-gas H_2 permeability of ≈100 Barrer and H_2/CO_2 selectivity of 20 at both dry and wet conditions for 100 h (Fig. 4d), which is the same as the initial H_2/CO_2 separation performance (Fig. 4a,b), indicating its robustness against physical aging and water vapor. The results also indicate that the deposited AlO_x layer is stable under high-temperature humid conditions.

Fig. 4e compares PBI-1C and PBI-17C with the leading polymeric materials for H_2/CO_2 separation [27,28,33,37,38,41,42,44–48]. PBI-1C displays superior H_2/CO_2 separation performance due to the fine-tuned polymer chain structures by AlO_x deposition and TMA cross-linking. With only 1 ALD cycle but significantly improved separation performance, the ALD technology is facile and scalable and holds great potential for industrial H_2/CO_2 separation.

4. Conclusion

We demonstrate a facile and scalable ALD approach to improve H_2/CO_2 selectivity and unexpectedly enhanced H_2 permeability in PBI. In addition to the deposition of AlO_x on the surface, the ALD allows the infiltration of the TMA into the films and reaction with the PBI chains synergistically to modify the free volumes at a sub-nanometer scale. Specifically, the infiltrated TMA reacts with the amine groups on the PBI chains, forming AlOx networks, disrupting the chain packing (increasing gas diffusivity) and reducing the free volume (increasing size-sieving ability). Impressively, one ALD cycle increases H_2 permeability by 120 % from 50 to 110 Barrer and H_2/CO_2 selectivity by 27 % from 15 to 19 at 200 °C. PBI-1C demonstrates stable and excellent H_2/CO_2 separation performance against high temperatures, water vapor, and physical aging, and it surpasses most state-of-the-art polymeric membranes and the permeability/selectivity upper bound. This study demonstrates that the few-cycle ALD can be an effective strategy to nanoengineer polymeric membranes for various molecular separations. The scalable yet effective fine-tuning of nanopores by few-cycle ALD may be used to manipulate porous materials for other applications, such as adsorption, catalysts, and energy storage.

5. Notes

The authors have filed a provisional patent application.

Declaration of competing interest

The authors declare that they have no known competing financial interests or personal relationships that could have appeared to influence the work reported in this paper.

Data availability

Data will be made available on request.

Acknowledgements

This work was funded by the U.S. Department of Energy (DOE) awards of DE-FE0031636 and DE-FE0032209. This research used the Materials Synthesis and Characterization and Electron Microscopy Facilities of the Center for Functional Nanomaterials, which is a U.S. DOE Office of Science User Facility, at Brookhaven National Laboratory under Contract No. DE-SC0012704.

Appendix A. Supplementary data

Supporting Information is available from the Wiley Online Library or from the authors. Supplementary data to this article can be found online at https://doi.org/10.1016/j.cej.2023.147401.

References

[1] A.H. Behroozi, V. Vatanpour, L. Meunier, M. Mehrabi, E.H. Koupaie, Membrane fabrication and modification by atomic layer deposition: processes and applications in water treatment and gas separation, ACS Appl. Mater. Interfaces 15 (2023) 13825–13843.
[2] S. Xiong, X. Qian, Z. Zhong, Y. Wang, Atomic layer deposition for membrane modification, functionalization and preparation: A review, J. Membr. Sci. 658 (2022), 120740.
[3] B. Gupta, M.A. Hossain, A. Riaz, A. Sharma, D. Zhang, H. Tan, C. Jagadish, K. Catchpole, B. Hoex, S. Karuturi, Recent advances in materials design using atomic layer deposition for energy applications, Adv. Funct. Mater. 32 (2022) 2109105.
[4] X. Yang, A.B.F. Martinson, J.W. Elam, L. Shao, S.B. Darling, Water treatment based on atomically engineered materials: Atomic layer deposition and beyond, Matter 4 (2021) 3515–3548.
[5] X. Yang, P. Sun, H. Zhang, Z. Xia, R.Z. Waldman, A.U. Mane, J.W. Elam, L. Shao, S. B. Darling, Polyphenol-sensitized atomic layer deposition for membrane interface hydrophilization, Adv. Funct. Mater. 30 (2020) 1910062.
[6] J. Lu, Y. Li, W. Song, M.D. Losego, R. Monikandan, K.I. Jacob, R. Xiao, Atomic Layer Deposition onto Thermoplastic Polymeric Nanofibrous Aerogel Templates for Tailored Surface Properties, ACS Nano 14 (2020) 7999–8011.
[7] Y. Liu, E.K. McGuinness, B.C. Jean, Y. Li, Y. Ren, B.G.d. Rio, R.P. Lively, M.D. Losego, R. Ramprasad, Vapor-Phase Infiltration of Polymer of Intrinsic Microporosity 1 (PIM-1) with Trimethylaluminum (TMA) and Water: A Combined Computational and Experimental Study, J. Phys. Chem. B, 126 (2022) 5920-5930.
[8] X. Zhou, M. Heiranian, M. Yang, R. Epsztein, K. Gong, C.E. White, S. Hu, J.H. Kim, M. Elimelech, Selective Fluoride Transport in Subnanometer TiO_2 Pores, ACS Nano 15 (2021) 16828–16838.
[9] X. Ma, P. Kumar, N. Mittal, A. Khlyustova, P. Daoutidis, K.A. Mkhoyan, M. Tsapatsis, Zeolitic imidazolate framework membranes made by ligand-induced permselectivation, Science 361 (2018) 1008–1011.
[10] E.K. McGuinness, F. Zhang, Y. Ma, R.P. Lively, M.D. Losego, Vapor phase infiltration of metal oxides into nanoporous polymers for organic solvent separation membranes, Chem. Mater. 31 (2019) 5509–5518.
[11] J. Nikkola, J. Sievanen, M. Raulio, J. Wei, J. Vuorinen, C. Tang, Surface modification of thin film composite polyamide membrane using atomic layer deposition method, J. Membr. Sci. 450 (2014) 174–180.
[12] Z. Zhang, A. Simon, C. Abetz, M. Held, A.-L. Höhme, E.S. Schneider, T. Segal-Peretz, V. Abetz, Hybrid Organic–Inorganic–Organic Isoporous Membranes with Tunable Pore Sizes and Functionalities for Molecular Separation, Adv. Mater. 33 (2021) 2105251.
[13] F. Li, L. Li, X. Liao, Y. Wang, Precise pore size tuning and surface modifications of polymeric membranes using the atomic layer deposition technique, J. Membr. Sci. 385 (2011) 1–9.
[14] E. Jeong, Y. Jeon, S. Cho, K. Choi, Textile-based washable polymer solar cells for optoelectronic modules: Toward self-powered smart clothing, Energy Environ. Sci. 12 (2019) 1878–1889.
[15] K.J. Dusoe, X. Ye, K. Kisslinger, A. Stein, S.-W. Lee, C.-Y. Nam, Ultrahigh elastic strain energy storage in metal-oxide-infiltrated patterned hybrid polymer nanocomposites, Nano Lett. 17 (2017) 7416–7423.
[16] D. Chen, J. Liang, C. Liu, G. Saldanha, F. Zhao, K. Tong, J. Liu, Q. Pei, Thermally stable silver nanowire–polyimide transparent electrode based on atomic layer deposition of zinc oxide on silver nanowires, Adv. Funct. Mater. 25 (2015) 7512–7520.
[17] B. Jin, K. Wang, H. Yu, X. He, X. Liang, Engineering oxygen vacancy-rich CeO_x overcoating onto Ni/Al_2O_3 by atomic layer deposition for bi-reforming of methane, Chem. Eng. J. 459 (2023), 141611.
[18] X. Niu, G. Dong, D. Li, Y. Zhang, Y. Zhang, Atomic layer deposition modified PIM-1 membranes for improved CO_2 separation: A comparative study on the microstructure-performance relationships, J. Membr. Sci. 664 (2022), 121103.
[19] L. Zhu, L. Huang, S.R. Venna, A. Blevins, Y. Ding, D. Hopkinson, M.T. Swihart, H. Lin, Scalable Polymeric Few-Nanometer Organosilica Membranes for Pre-Combustion CO_2 Capture, ACS Nano 15 (2021) 12119–12128.
[20] L. Hu, V.T. Bui, N. Esmaeili, H. Lin, Nanoengineering membrane surfaces: A new paradigm for efficient CO_2 capture, Carbon Capture Sci. Tech. 10 (2024), 100150.
[21] M.D. Groner, S.M. George, R.S. McLean, P.F. Carcia, Gas diffusion barriers on polymers using Al_2O_3 atomic layer deposition, Appl. Phys. Lett. 88 (2006), 051907.
[22] O. Toikkanen, M. Nisula, E. Pohjalainen, S. Hietala, H. Havansi, J. Ruotsalainen, S. Halttunen, M. Karppinen, T. Kallio, Al_2O_3 coating grown on Nafion membranes by atomic layer deposition, J. Membr. Sci. 495 (2015) 101–109.
[23] D.-W. Choi, H. Park, J.H. Lim, T.H. Han, J.-S. Park, Three-dimensionally stacked Al2O3/graphene oxide for gas barrier applications, Carbon 125 (2017) 464–471.
[24] X. Chen, L. Wu, H. Yang, Y. Qin, X. Ma, N. Li, Tailoring the microporosity of polymers of intrinsic microporosity for advanced gas separation by atomic layer deposition, Angew. Chem. Int. Ed. 60 (2021) 17875–17880.
[25] L. Hu, S. Pal, H. Nguyen, V. Bui, H. Lin, Molecularly Engineering Polymeric Membranes for H_2/CO_2 Separation at 100–300 °C, J. Polym. Sci. 58 (2020) 2467–2481.
[26] Y. Han, W.S. Ho, Polymeric membranes for CO_2 separation and capture, J. Membr. Sci. 628 (2021), 119244.

[27] J. Wu, C. Liang, A. Naderi, T. Chung, Tunable Supramolecular Cavities Molecularly Homogenized in Polymer Membranes for Ultraefficient Precombustion CO_2 Capture, Adv. Mater. 34 (2021) 2105156.
[28] L. Zhu, M.T. Swihart, H. Lin, Unprecedented Size-Sieving Ability in Polybenzimidazole Doped with Polyprotic Acids for Membrane H_2/CO_2 Separation, Energy Environ. Sci. 11 (2018) 94–100.
[29] R. Hardian, P. Pogany, Y. Lee, G. Szekely, Molecular sieving using metal–polymer coordination membranes in organic media, J. Mater. Chem. A 9 (2021) 14400–14410.
[30] A. Subramanian, G. Doerk, K. Kisslinger, H.Y. Daniel, R.B. Grubbs, C.-Y. Nam, Three-dimensional electroactive ZnO nanomesh directly derived from hierarchically self-assembled block copolymer thin films, Nanoscale 11 (2019) 9533–9546.
[31] C.A. Wilson, R.K. Grubbs, S.M. George, Nucleation and growth during Al_2O_3 atomic layer deposition on polymers, Chem. Mater. 17 (2005) 5625–5634.
[32] C.Z. Leng, M.D. Losego, Vapor phase infiltration (VPI) for transforming polymers into organic–inorganic hybrid materials: a critical review of current progress and future challenges, Mater. Horiz. 4 (2017) 747–771.
[33] L. Hu, V.T. Bui, S. Pal, W. Guo, A. Subramanian, K. Kisslinger, S. Fan, C.Y. Nam, Y. Ding, H. Lin, In Situ Growth of Crystalline and Polymer-Incorporated Amorphous ZIFs in Polybenzimidazole Achieving Hierarchical Nanostructures for Carbon Capture, Small 2201982 (2022).
[34] L. Hu, V.T. Bui, A. Krishnamurthy, S. Fan, W. Guo, S. Pal, X. Chen, G. Zhang, Y. Ding, R.P. Singh, M. Lupion, H. Lin, Tailoring Sub-3.3 Å Ultramicropores in Advanced Carbon Molecular Sieve Membranes for Blue Hydrogen Production, Sci. Adv. 8 (2022) eabl8160.
[35] P.R. Bevington, D.K. Robinson, Data Reduction and Error Analysis for the Physical Sciences, 2nd ed., McGraw-Hill Inc, New York, 1992.
[36] M. Omidvar, H. Nguyen, L. Huang, C.M. Doherty, A.J. Hill, C.M. Stafford, X. Feng, M.T. Swihart, H. Lin, Unexpectedly Strong Size-Sieving Ability in Carbonized Polybenzimidazole for Membrane H_2/CO_2 Separation, ACS Appl. Mater. Interfaces 11 (2019) 47365–47372.
[37] L. Hu, V.T. Bui, L. Huang, R.P. Singh, H. Lin, Facilely Cross-linking Polybenzimidazole with Polycarboxylic Acids to Improve H_2/CO_2 Separation Performance, ACS Appl. Mater. Interfaces 13 (2021) 12521–12530.
[38] L. Zhu, M.T. Swihart, H. Lin, Tightening Polybenzimidazole (PBI) Nanostructure via Chemical Cross-Linking for Membrane H2/CO2 Separation, J. Mater. Chem. A 5 (2017) 19914–19923.
[39] T. Yang, Y. Xiao, T.S. Chung, Poly-/metal-benzimidazole nano-composite membranes for hydrogen purification, Energy Environ. Sci. 4 (2011) 4171–4180.
[40] G.N. Parsons, S.E. Atanasov, E.C. Dandley, C.K. Devine, B. Gong, J.S. Jur, K. Lee, C. J. Oldham, Q. Peng, J.C. Spagnola, Mechanisms and reactions during atomic layer deposition on polymers, Coord. Chem. Rev. 257 (2013) 3323–3331.
[41] L. Hu, V.T. Bui, S. Fan, W. Guo, S. Pal, Y. Ding, H. Lin, Supramolecular assemblies of polybenzimidazole and aromatic polycarboxylic acids with superior mechanical and H_2/CO_2 separation properties, J. Mater. Chem. A 10 (2022) 10872–10879.
[42] J. Wu, T. Chung, Supramolecular Polymer Network Membranes with Molecular-Sieving Nanocavities for Efficient Pre-Combustion CO_2 Capture, Small Methods 6 (2021) 2101288.
[43] L. Hu, S. Fan, L. Huang, V.T. Bui, T. Tran, K. Chen, Y. Ding, M.T. Swihart, H. Lin, Supramolecular polymer networks of ion-coordinated polybenzimidazole with simultaneously improved H_2 permeability and H_2/CO_2 selectivity, Macromolecules 55 (2022) 6901–6910.
[44] A. Naderi, A.A. Tashvigh, T. Chung, H_2/CO_2 Separation Enhancement via Chemical Modification of Polybenzimidazole Nanostructure, J. Membr. Sci. 572 (2019) 343–349.
[45] M. Omidvar, C.M. Stafford, H. Lin, Thermally Stable Cross-Linked P84 with Superior Membrane H_2/CO_2 Separation Properties at 100 ^{o}C, J. Membr. Sci. 575 (2019) 118–125.
[46] Z. Ali, F. Pacheco, E. Litwiller, Y. Wang, Y. Han, I. Pinnau, Ultra-Selective Defect-Free Interfacially Polymerized Molecular Sieve Thin-Film Composite Membranes for H_2 Purification, J. Mater. Chem. A 6 (2018) 30–35.
[47] M. Shan, X. Liu, X. Wang, Z. Liu, H. Iziyi, S. Ganapathy, J. Gascon, F. Kapteijn, Novel High Performance Poly(p-Phenylene Benzobisimidazole) (PBDI) Membranes Fabricated by Interfacial Polymerization for H_2 Separation, J. Mater. Chem. A 7 (2019) 8929–8937.
[48] M. Shan, X. Liu, X. Wang, I. Yarulina, B. Seoane, F. Kapteijn, J. Gascon, Facile Manufacture of Porous Organic Framework Membranes for Precombustion CO_2 Capture, Sci. Adv. 4 (2018) eaau1698.